Leaky-wave radiating surface on heterogeneous high-κ material for monolithic antenna-frontend integration ⊘

Amirhossein Askarian ✉ iD ; Jianping Yao iD ; Zhenguo Lu iD ; Ke Wu iD

Check for updates

CrossMark

View Online   Export Citation

Articles You May Be Interested In

Photon beamline frontends for the PETRA III extension project

AIP Conference Proceedings (July 2016)

Commissioning of the synchrotron radiation protection system and beamlines frontends at NSLS-II

AIP Conference Proceedings (July 2016)

A low-noise analog frontend design for the Taiji phasemeter prototype

Rev Sci Instrum (May 2021)

Leaky-wave radiating surface on heterogeneous high-κ material for monolithic antenna-frontend integration

View Online   Export Citation   CrossMark

Amirhossein Askarian,[1,a] ID Jianping Yao,[2] ID Zhenguo Lu,[3] ID and Ke Wu[1] ID

AFFILIATIONS

[1]Poly-Grames Research Center and Department of Electrical Engineering, Polytechnique Montreal (University of Montreal), Montreal, Quebec H3T 1J4, Canada
[2]School of Electrical Engineering and Computer Science, University of Ottawa, Ottawa, Ontario K1N 6N5, Canada
[3]Advanced Electronics and Photonics Research Center the National Research Council Canada (NRC) Ottawa, Ontario K1A 0R6, Canada

[a]Author to whom correspondence should be addressed: a.askarian@polymtl.ca

ABSTRACT

In a highly integrated analog radio-over-fiber transceiver, seamless integration of the antenna-frontend is crucial as an antenna is generally implemented on a high-κ material, which is set to highly degrade the antenna's performance. This work is concerned with the radiation behavior improvement of a planar leaky-wave antenna with an inductive partially reflecting surface (PRS) on a high-κ substrate for the development of a highly directive antenna. To begin with, we show how a thin and single-mode resonance (SMR) inductive PRS on high-κ materials in a planar leaky-wave antenna is set to provoke two resonance frequencies (i.e., PRS and cavity resonances) to converge, thereby diminishing the antenna's broadside directivity. By applying an equivalent circuit model, we explain how a multi-mode resonance (MMR) PRS can adequately be applied to address the underlying challenges. Subsequently, the leaky-wave radiation behavior of an antenna with a heterogeneous substrate is investigated and analytical equations are derived and verified with a full-wave simulation. The effects of material permittivity and thickness in a heterogeneous-cavity antenna on leaky-wave performance are investigated using these approximate yet accurate-enough equations. To justify the findings, two 9×9 planar leaky-wave antennas are prototyped on heterogeneous substrates based on SMR and MMR PRS and the radiation performances are compared. Our investigations reveal that in the proposed scenario, an MMR PRS can significantly enhance the antenna's broadside directivity by over 4 dBi at the resonance frequency (27.5 GHz), which is also set to improve radiation pattern compared to a SMR-based antenna. Finally, a single-fed dual-band aperture-shared antenna with a large frequency ratio (S-band and Ka-band) is developed and fabricated on a high-κ substrate based on the proposed MMR PRS.

Published under an exclusive license by AIP Publishing. https://doi.org/10.1063/5.0136228

I. INTRODUCTION

The emerging demand for high-speed, efficient, and low-cost millimeter (mmW) wireless communications is enticing for antenna and RF circuit researchers and practitioners to design and develop appealing technical solutions in terms of efficiency, cost, and overall performance. The well-established analog radio-over-fiber (ARoF) technology, which has been around since 1983,[1,2] is a viable approach to establishing high-performance and broadband wireless connectivity with low expenditure as well as simplifying base station transceivers.[3]

Microwave photonics technology has empowered the development of different ARoF architecture including low footprint and efficient broadband or multiband fiber-wireless systems.[4–7] In a transceiver based on microwave photonics technology, RF signal generation, filtering, mixing, and phase-shifting are all handled in a highly efficient optical processor, which not only substantiates the degree of integration but also dramatically reduces the complexity, costs, and losses in the frontend. To preserve a high integration level and also to eliminate parasitic effects and losses associated with bonding wires, seamless integration of an antenna array with a photodiode is essential. Since high permittivity materials, such as

SiGe, InP, etc., are usually adopted to design a photodiode, the antenna-frontend integration inevitably encounters major hurdles for achieving broadband, highly efficient, and high-gain radiations.

Naturally, a highly directive and power efficient antenna array is required in the transceiver to compensate for the overall propagation loss in an mmW fiber-wireless communication. In addition, a dual-band antenna array with a high frequency ratio is necessary to exploit the microwave (MW) and mmW spectrums' potential advantages in order to establish both a highly reliable (given by MW signal) and broadband (offered by mmW signal) wireless connectivity.[8,9]

As suggested by the conceptual block diagram of a dual-band ARoF system based on microwave photonic in Fig. 1, a multi-wavelength quantum dot laser diode (MW-QDLD) is adopted in a central station to generate four high-resolution optical signals corresponding to $\{\lambda_1, \lambda_2, \lambda_3, \lambda_4\}$. Two RF signals are then modulated on the optical signals through an optical modulator. Four optical signals are set to beat on a photodiode at the access point to generate both MW and mmW RF signals for dual-band communications. Therefore, a dual-band antenna on a high-κ substrate is intended for seamless integration with a photodiode in the transceiver.

In this work, we aim to develop a dual-band with a large frequency ratio and high-gain antenna on a high-κ material for a dual-band ARoF wireless system, as conceptually illustrated in Fig. 1. Since this antenna is integrated with an MW-QDLD in an optoelectronic integrated circuit (OEIC), it should generally fulfill three major criteria, namely, (1) the antenna should have a highly directive radiation beam while it occupies a small real estate and has a low profile structure; (2) to facilitate antenna integration with the MW-QDLD through the OEIC fabrication process, the antenna should have a simple structure that also allows surface waves to be effectively suppressed or diminished without adding excessive complexity to the system; and (3) with reference to Fig. 1, for integration with an MW-QDL, the antenna should be able to operate on both frequency bands through a single feed line (single-fed dual-band antenna).

A review of recent publications[10–15] indicates a growing research interest in developing dual-band antennas having a large frequency ratio. However, low permittivity substrates have been used in those antenna structures as this common practice enables an easy generation of high efficiency radiation while restricting the antenna arrays from seamlessly integrating with active circuits. Considering the special requirement of high-κ substrate integration in this work, we will address both challenges, namely, (1) creating an antenna on a high-κ substrate with improved radiation performances and (2) devising a single-fed, dual-band, and high-gain antenna with a large frequency ratio suitable for seamless integration with an ARoF-based frontend.

For a variety of technical reasons, developing a conventional antenna array on a high-κ substrate is exceedingly challenging. First, a coupling of antenna elements through surface waves within a high-κ substrate results in various disastrous consequences such as excessive mutual coupling, poor radiation efficiency, and strong wave diffraction from truncated substrate's edges.[16–21] Then, a significant mismatch takes place between the antenna array aperture and air, resulting in a narrowband operation and poor radiation.[18] In addition, instead of yielding an adequate radiation, a tightly bound electromagnetic (EM) wave is formed in a high-κ substrate, degrading the antenna's performance.

To address these concerns, various strategies were studied and presented in the literature.[16–22–28] Although these solutions are practical and adaptable, they may increase the cost, footprint, and complexity of the antenna array in question, thus introducing a new set of issues and problems for circuit-antenna integration.

Planar leaky-wave antenna, also known as a Fabry–Pérot cavity antenna, is a suitable alternative for conventional array antennas since a highly directive pencil beam can be easily realized with a spartan structure.[28–36] This radiating structure, which is typically realized by two parallel metallic plates [ground plane and partially reflecting surface (PRS)] positioned roughly a half-wavelength apart, can be efficiently excited by a magnetic or electric current (slot or dipole) etched on one surface or placed in between two plates, respectively. In such antenna architecture, surface waves are either suppressed or weakly excited on the antenna's aperture due to a boundary condition imposed by a metallic PRS, which presents potentially an advantage for developing a high-gain antenna on a high-κ substrate.

Therefore, in this paper, we intend to deploy a planar leaky-wave antenna with an inductive PRS[32] as it enables us to effectively reuse antenna aperture over two different frequency bands due to the fact that the real estate is a crucial factor in an integrated antenna design.
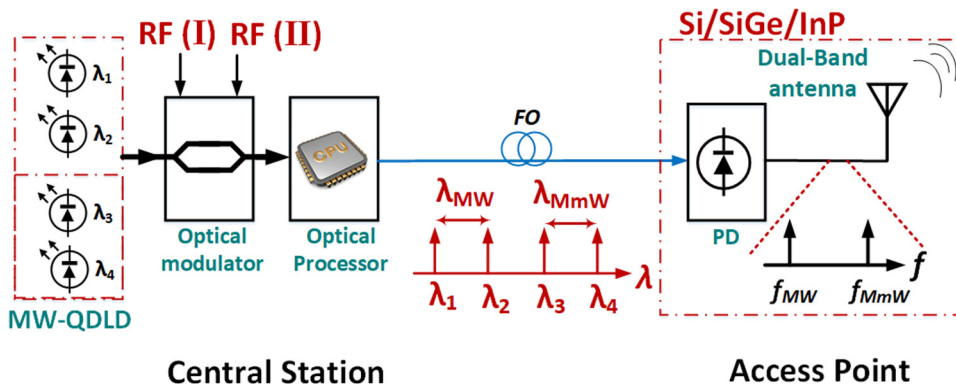
FIG. 1. General block diagram of a typical dual-band ARoF system.

To begin with, we investigate the issue regarding the use of a conventional thin single-mode resonance (SMR) surface on a high-κ substrate by developing an equivalent circuit model (ECM). As the relative permittivity of the cavity increases in an antenna with an SMR PRS, the PRS becomes more transparent, resulting in a gain loss for the antenna. Although increasing the susceptance of the PRS (e.g., using a narrower slot in this work) could be a potential solution for some structures, it is not always a practical and feasible solution due to fabrication process constraints and restrictions for satisfying the cavity's resonant condition. To address this fundamental issue and to propose a general methodology, we examine the application of the multi-mode resonance (MMR) concept for improving antenna radiation performances on a high- substrate. We show that MMR PRS can not only fix this problem but also improve antenna gain bandwidth.

Subsequently, a planar leaky-wave theory is applied to explore and analyze a double-layered substrate integrated cavity realizing a heterogeneous antenna-frontend integration.

Our investigations show that adding a layer with a lower relative permittivity over the primary substrate (feeding network layer hosting active circuits) with a large permittivity brings up some privileges in antenna design. This method not only makes it easier to select a proper material for satisfying the cavity resonance at a desired frequency but also provides more control over the phase and attenuation constants of leaky waves.

II. THEORY AND FUNDAMENTAL ISSUES

The magnitude of the reflection coefficient of PRS with respect to the relative permittivity of a cavity, which is evaluated by (1) and ECM, is described in Fig. 2 for certain values of the normalized PRS susceptance $|B_{PRS}\eta_0|$. It shows the effect of a relative dielectric permittivity inside a cavity on the magnitude of the PRS reflection coefficient.

As depicted in Fig. 2, for a practical and high-gain antenna with $|\Gamma_{PRS}| > 0.85$[29] corresponding to $|\bar{B}_{PRS}| = |B_{PRS}\eta_0| > 6$, as the permittivity of the dielectric inside the cavity is increased, the
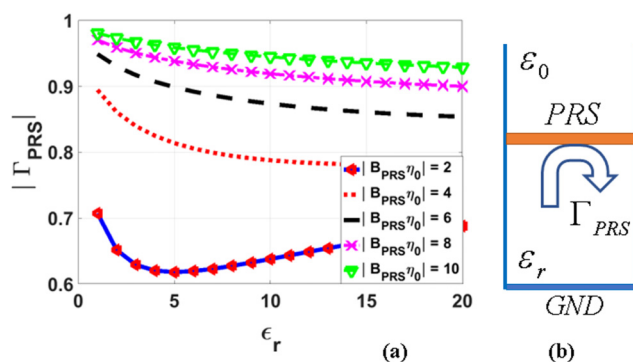

FIG. 2. (a) Variations of magnitude of PRS reflection coefficient, evaluated in the air-PRS boundary, for some values of normalized PRS susceptance with respect to relative permittivity of the material inside the cavity, and (b) ECM of thin and SMR-based antennas.

magnitude of the PRS reflection coefficient is diminished for each value of $|\bar{B}_{PRS}|$. This would result in a tangible gain loss in radiation,[30–32] particularly, for a lower value of $|B_{PRS}\eta_0|$. To reach a robust conclusion about radiation behavior, the resonance condition inside the cavity should be properly considered as the PRS's susceptance plays a significant role in the resonance conditions inside the cavity at the desired frequency. A well-known ray-optic approach is used to calculate the desired phase of the PRS reflection coefficient (hereinafter referred to as "PRS phase" or "φ^{PRS}") for satisfying the resonance criteria inside the cavity for maximum broadside radiation, as described in Eq. (2).[33]

In addition, the required height for satisfying the cavity resonance conditions with an inductive PRS is evaluated by (3).[32] Substituting (3) in Eq. (2), the PRS phase can be obtained alternatively by (4) for the fundamental resonance mode [corresponding to $n = 0$ in Eq. (2)] in the cavity. Equation (4) states the required PRS phase for fulfilling the cavity resonance condition as a function of the magnitude of normalized PRS susceptance $|\bar{B}_{PRS}|$ and relative permittivity ε_r.

It is worth noting that in a planar leaky-wave antenna, two resonant frequencies contribute to the operation, notably (1) cavity resonance frequency, corresponding to a frequency at which (2)–(4) are satisfied.[32,33] In other words, the cavity starts to resonate when φ^{PRS} is set to satisfy (2) or (4) or the cavity height satisfies (3); (2) the PRS resonance frequency, corresponding to a frequency at which φ^{PRS} vanishes and the magnitude of the reflection coefficient is also drastically decreased (i.e., PRS becomes transparent),

$$|\Gamma_{PRS}| = \sqrt{\frac{\left(1 - \sqrt{\varepsilon_r}\right)^2 + |\bar{B}_{PRS}|^2}{\left(1 + \sqrt{\varepsilon_r}\right)^2 + |\bar{B}_{PRS}|^2}}, \quad (1)$$

$$\varphi_{PRS} = 4\pi \frac{h}{\lambda_g} + (2n - 1)\pi \quad n = 0, \pm 1, \pm 2, \ldots, \quad (2)$$

$$\frac{h}{\lambda_g} = \frac{1}{2}\left(1 - \frac{\sqrt{\varepsilon_r}}{\pi|\bar{B}_{PRS}|}\right), \quad (3)$$

$$\varphi^{PRS} = \pi - \frac{2\sqrt{\varepsilon_r}}{|\bar{B}_{PRS}|}. \quad (4)$$

To understand the role of relative permittivity of a substrate in the performance of a dielectric-filled planar leaky-wave antenna with an inductive PRS, a 3D plot of (4) for a wide range of permittivity ($1 \leq \varepsilon_r \leq 50$) and normalized PRS susceptance ($4 \leq |\bar{B}_{PRS}| \leq 50$) is provided in Fig. 3. Evidently, in a PRS (constant $|\bar{B}_{PRS}| = |B_{PRS}\eta_0|$ planes), $\partial\varphi_{PRS}/\partial\varepsilon_r < 0$, the latter means that the PRS phase (φ_{PRS}) should decrease to maintain the resonance condition [satisfying (4)] at the cavity's resonant frequency when the permittivity of the substrate inside the cavity increases. Equivalently, as the relative permittivity is increased inside the cavity, the PRS resonance frequency [corresponding to a frequency at which $\varphi_{res.}^{PRS} = 0$, cf. Fig. 4(d)] approaches the cavity resonance frequency. In this case, the magnitude of the reflection coefficient
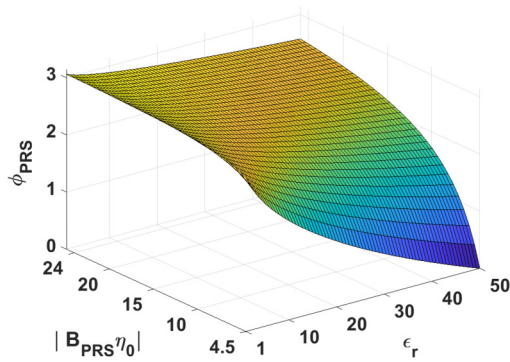
FIG. 3. 3D plot of φ_{PRS} [mentioned in Eq. (4)] with respect to variations of relative permittivity and normalized PRS susceptance.

also decreases and the PRS becomes more transparent, which results in a gain loss in the antenna.

Therefore, to avoid such a gain loss, the cavity resonance frequency should be properly adjusted so as to stay far away from the PRS resonance frequency. To validate the analytical results, the Ansys HFSS is used to perform a full-wave analysis on a typical thin and SMR PRS. Although this analysis is applicable to a wide range of inductive PRS, a PRS with cross-slot unit cells [cf. Fig. 4(a)] on Rogers RT/duroid 6006 with $\varepsilon_r = 6.15$ is used for proof of concept in this work. As shown in Fig. 4(a), a port is assigned at the bottom of a unit cell. Having de-embedded the dielectric thickness, we calculated the normalized input impedance along with the magnitude and phase of the reflection coefficient of the PRS in the desired frequency range as shown in Figs. 4(b)–4(d) in which PRS and cavity resonances are also indicated.

According to Fig. 4(d) and the theory of planar leaky-wave antenna, the cavity resonance is the point at which two curves get coincided, namely, the curve obtained by (2) and the phase of reflection coefficient obtained by HFSS. At this resonant frequency,

the normalized PRS susceptance is evaluated about $|\bar{B}_{PRS}| = 5.5$ by HFSS.

To investigate and validate the effects of relative permittivity on the PRS performance, the normalized input impedance and magnitude and phase of the reflection coefficient of the PRS unit-cell are examined by HFSS for three different relative permittivity values, namely, $\varepsilon_r = 2.2$, 6.15, and 10.2, as shown in Figs. 5(a)–5(c). The cavity resonance is determined by (2) and (3) with $|\bar{B}_{PRS}| = 5.5$. The relative permittivity of the cavity is swept in this case, while the PRS dimensions remain unchanged. Note that, as the permittivity changes, the cavity height is adjusted in accordance with (3) to maintain the cavity resonance at the desired frequency (i.e., 27.5 GHz). As the substrate permittivity rises from 2.2 to 10.2, the PRS resonance frequency [indicated in Figs. 5(a) and 5(c)] approaches the cavity resonance frequency (i.e., 27.5 GHz).

In this case, according to Fig. 5(c), the magnitude of the reflection coefficient of PRS at cavity resonance is diminished; therefore, PRS becomes gradually transparent at cavity resonance frequency as the substrate permittivity is increased, which generally agrees with the results shown in Fig. 2. At the same time, the phase of the reflection coefficient in Fig. 5(a) at cavity resonance is decreased, implying that the PRS resonance approaches the cavity resonance, which results in low-gain radiation, as discussed earlier.

This is consistent with the theory elaborated by (2)–(4) in this section along with Fig. 3, which introduces a fundamental challenge in the design of a high-gain planar leaky-wave antenna in a high-κ substrate.

Note that, as expected, the impedance bandwidth of PRS is also decreased as the permittivity of substrate is increased. To circumvent this scenario, an MMR PRS is proposed and investigated in Sec III.

III. MULTI-MODE RESONANCE ANTENNA

The MMR concept was used in the antenna and filter design to enhance their performance.[37–40] In this section, an MMR PRS is designed to address the fundamental issue of the SMR counterpart
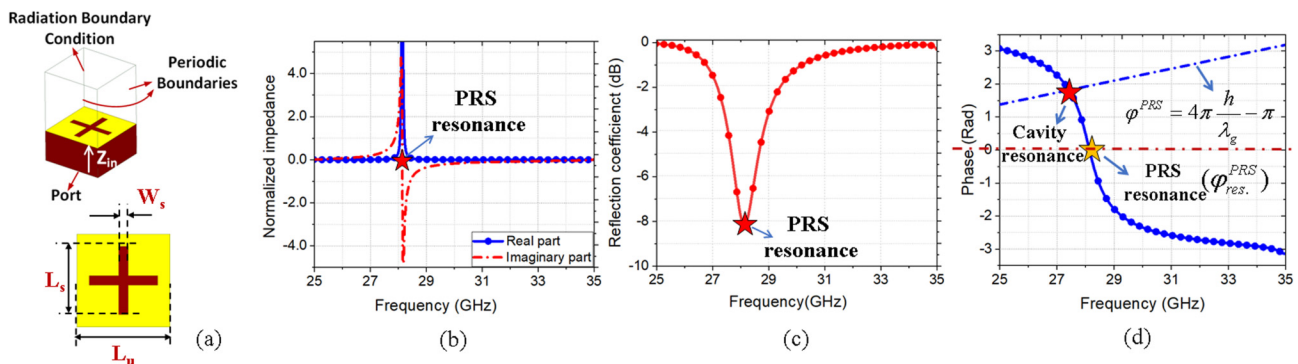

FIG. 4. (a) Unit-cell and top view of a cross-slot SMR PRS (Ws = 0.4 mm, Ls = 3.6 mm, Lu = 4.9 mm, $\varepsilon_r = 6.15$), (b) normalized input impedance (normalized to air impedance, η_0), (c) magnitude of reflection coefficient, and (d) phase of reflection coefficient of cross-slot SMR PRS.
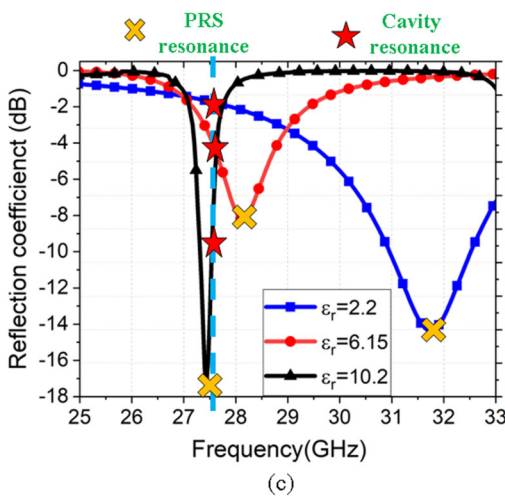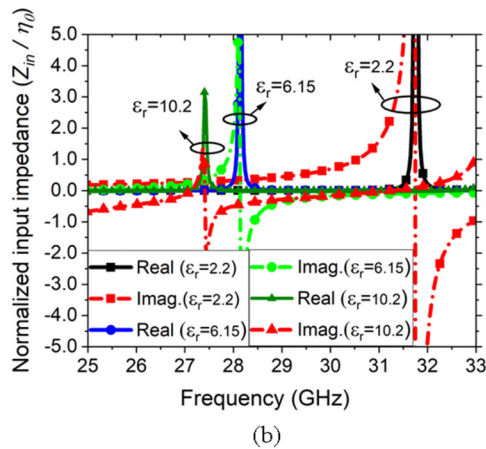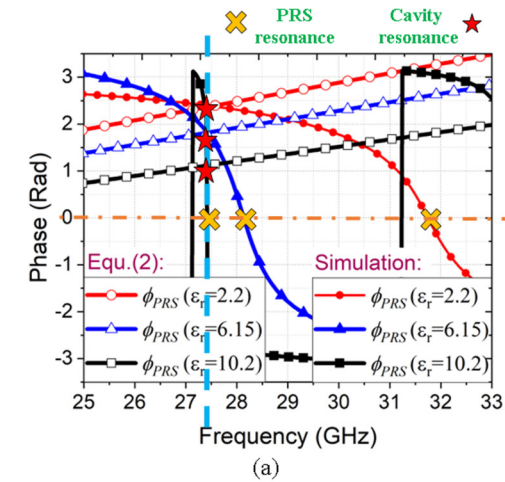
(a)

(b)

FIG. 5. (a) PRS phase evaluated by HFSS and (2), (b) normalized input imped-ance (normalized to air impedance η_0), and (c) magnitude of reflection coeffi-cient of SMR PRS for three different values of the relative permittivity (cavity resonates at 27.5 GHz as indicated by a dashed line in these figures).
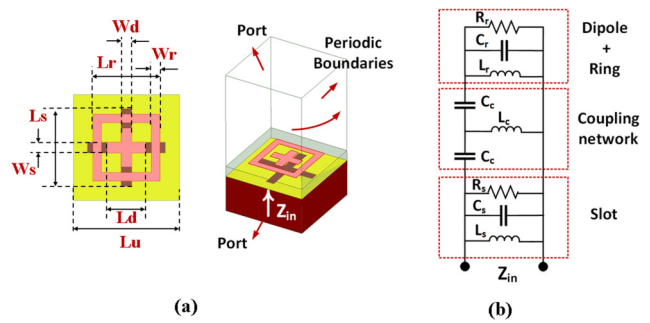

(a)   (b)

FIG. 6. (a) Unit-cell (Ls = 3.6 mm, Ws = 0.4 mm, Lr = 3.1 mm, Wr = 0.4 mm, Ld = 1.8 mm, Wd = 0.5 mm, Lu = 4.9 mm, ϵ_r = 6.15), and (b) ECM of the pro-posed MMR PRS, L_s = 11.97 pH, C_s = 2.95 pF, R_s = 374.62 Ω, C_c = 0.55 pF, L_c = 293.3 pH, R_r = 10 kΩ, C_r = 1 pF, L_r = 17.64 pH.

and to increase the directivity of a planar leaky-wave antenna on a high-κ substrate.

To construct an MMR PRS, a short cross-dipole inside a square ring is printed on a dielectric slab (Rogers RT/duroid 6006 used in this work) and placed on the top of an SMR PRS, as illus-trated in Fig. 6(a). The ECM of cross short dipoles and square ring can be totally described by a parallel RLC circuit and the ECM of the cross-slot in the bottom layer is also equivalent to a parallel RLC circuit as illustrated in Fig. 6(b). A T-shaped equivalent network between two resonant tank circuits models the EM mutual coupling between two RLC circuits. Circuit component values are obtained with the help of Advanced Design System (ADS) software and are mentioned in Fig. 6(b).

The S-parameters of the MMR PRS are evaluated by assigning two ports at the top and bottom of the unit-cell [cf. Fig. 6(a)] and de-embedding the corresponding air and dielectric spaces at the top and bottom, respectively. Dimensions in both slot and ring-dipole layers are then optimized to create multimode resonances over the frequency band of interest. The normalized input imped-ances evaluated by the full-wave simulation in HFSS and the circuit model in ADS are depicted in Fig. 7(a), also the magnitude of both reflection and transmission coefficients are plotted in Fig. 7(b).

With reference to Fig. 7(b), two PRS resonance frequencies appear around 25.5 and 34 GHz corresponding to two nulls on the curve of the reflection coefficient. Between these two frequencies, the reflection coefficient is constant and remains around unity realizing an opaque PRS. Looking into the impedance curve in Fig. 7(a), the capacitive effect of the first resonance is offset by the inductivity of the second resonance in the region between two PRS resonance frequencies and appropriately far away from them, resulting in a frequency band with low resistance (R) and reactance (X) values with negligible variations over the frequency range. Therefore, PRS susceptance can be estimated as $|\bar{B}_{PRS}| \approx |1/\bar{X}_{PRS}|$. Since $\bar{X}_{PRS}$ is very small between the two resonance frequencies, the corresponding realized susceptance ($\bar{B}_{PRS}$) would be large. Simulation results show that the PRS susceptance is as large as $|\bar{B}_{PRS}^{MMR}| \approx 25.5$ at 27.5 GHz, which is much larger than that of the SMR antenna with $|\bar{B}_{PRS}^{SMR}| = 5.5$.
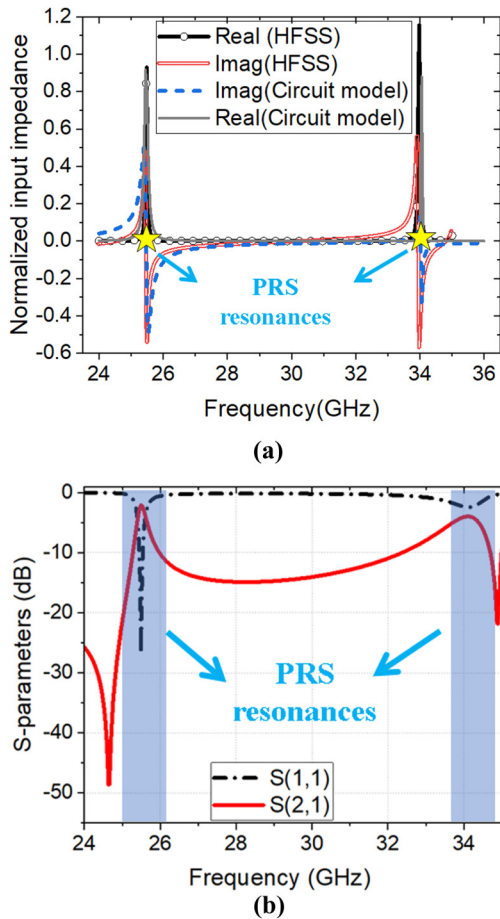
(a)

(b)

FIG. 7. (a) Normalized input impedance (normalized to air impedance η_0) evaluated by full wave simulation in HFSS and circuit model in ADS; (b) magnitude of the reflection coefficient of the MMR antenna shown in Fig. 6.

In this context according to the theory of planar leaky-wave antenna, a larger value of normalized PRS susceptance $|\bar{B}_{PRS}|$ results in a higher antenna peak field value at broadside.[32] As a result, MMR PRS can enhance broadside radiation since it provides a greater $|\bar{B}_{PRS}|$ than SMR PRS. The cavity resonance frequency can be set in the region between two PRS resonances by appropriately adjusting the cavity height. In this case, according to Figs. 2 and 3, due to the large value of $|\bar{B}_{PRS}|$, the magnitude and phase of the PRS reflection coefficient would experience minor changes as the permittivity of the cavity increases. This characteristic makes the MMR PRS suited for achieving high-gain leaky-wave radiation in an antenna on a material with high relative permittivity.

Consequently, an MMR PRS provides (1) an opaque PRS with a larger reflection coefficient than that of SMR PRS on a high-κ material, as shown in Fig. 7(b); therefore, realized leaky-wave attenuation constant (α) would be small (as studied in Sec. IV), and as a result, broadside directivity ($D \propto 1/\bar{\alpha}^2$) and power density at broadside are increased according to (5)[32,35] and (2) a larger value of
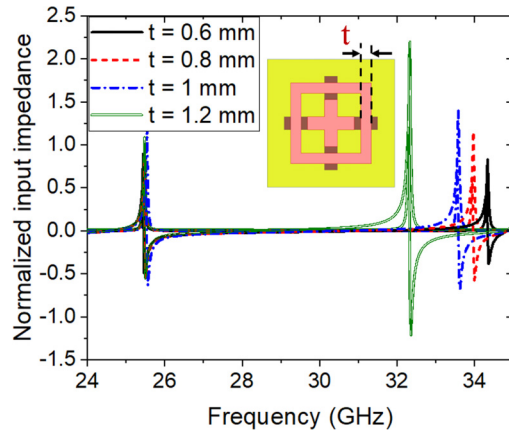

FIG. 8. Variations of normalized input impedance (normalized to air impedance η_0), of MMR PRS with respect to "t."

$|\bar{B}_{PRS}^{MMR}| = 25.5$ in comparison to the SMR counterpart with $|\bar{B}_{PRS}^{SMR}| = 5.5$ on a high-κ substrate; in this case, according to (6), the broadside peak field value is also increased,[32]

$$\text{Maximum broadside power density} = \frac{4\mu_r \sqrt{\varepsilon_r \mu_r}}{\pi} \frac{1}{\bar{\alpha}^2}, \quad (5)$$

$$\text{Normalized peak field value at broadside} = \frac{2|\bar{B}_{PRS}|}{\sqrt{\varepsilon_r}}, \quad (6)$$

where ε_r and μ_r are relative permittivity and permeability of the material inside the cavity and $\bar{\alpha} = \alpha/k_0$ is the normalized leaky-wave attenuation constant.

Parametric studies are performed to investigate MMR behaviors, as illustrated in Figs. 8 and 9. In Fig. 8, the outer edge of the
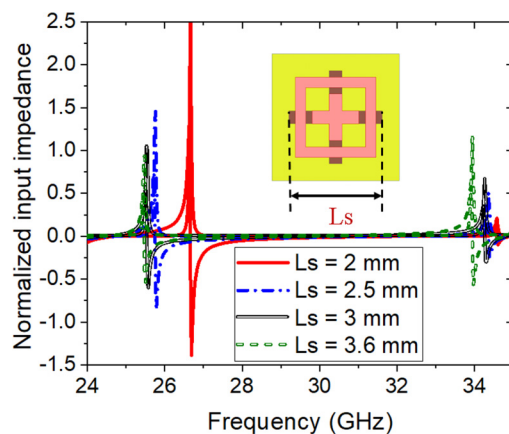

FIG. 9. Variations of normalized input impedance (normalized to air impedance η_0) of MMR PRS with respect to "Ls."

square ring is swept while the inner edge remains fixed. Therefore, the width of the square ring at the top layer changes while the gap between the square ring and cross-dipole is kept constant. In this case, the inductivity of the square ring is changed while the coupling capacitance between the cross-dipole and square ring remains unchanged. As shown in the figure, the second resonance is changed while the first resonance is almost fixed around 25.5 GHz. The same results are observed by changing the inside edge of the square ring, which are not discussed here for brevity. By altering the length of the cross-slot in the bottom layer as shown in Fig. 9, both resonances are swept along the frequency axis, signifying that the coupling between two resonator circuits is changed by altering the slot length.

IV. DESIGN PROCEDURE AND ANALYSIS

In this section, we aim to design two antennas with SMR and MMR PRSs at 27.5 GHz and analyze them by equivalent transmission lines (TLs) model to illustrate and support the theory presented and discussed in the previous sections. In addition, this model provides a general design methodology as well as a leaky-wave analysis of the antenna with a heterogeneous cavity, and then a full-wave simulation validates the results.

A. Antenna with heterogeneous cavity

Generally, a heterogeneous dielectric can be practically realized by a stack of several dielectric layers having different properties such as relative permittivity, permeability, and thickness. This is significant in ARoF integrated design scenarios as materials generally employed in electro-optical transceivers are not necessarily the same as that used in RF circuits' and antennas' development. Also, it is of practical interest in planar leaky-wave antenna design as this technique adds more degrees of freedom in the cavity design with available commercial substrates. In this work, we utilize a double-layer planar leaky-wave antenna in which the substrate used in the feeding layer is not the same as that used in the radiating layer. The transverse TL model of an antenna with a double-layer cavity is used for design and analysis as shown in Fig. 10. Note that this model would be more accurate when the incidence wave impinges at the same angle as the one used for the PRS characterization[41] which is $\theta = 0$.
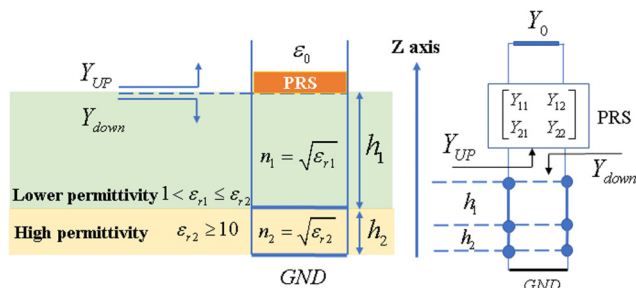

FIG. 10. TL model of the planar leaky-wave antenna with double-layer cavity (i.e., a heterogeneous cavity).
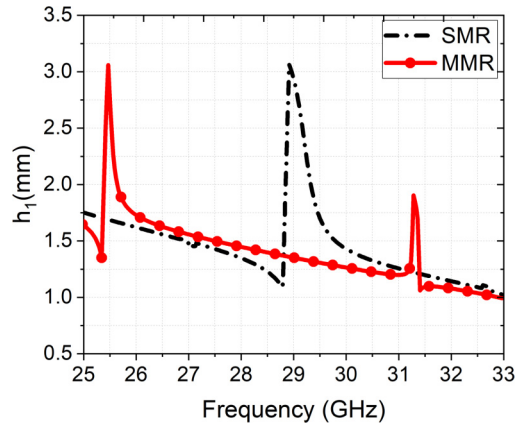

FIG. 11. Calculated "h_1" (cf. Fig. 10) by (8) vs frequency for antennas with SMR and MMR PRSs.

To mimic a practical integrated antenna-frontend design scenario in a ARoF system,[4] a relatively thin dielectric with a large relative permittivity (Rogers 6010, $\varepsilon_r = 10.2$, $h_2 = 0.635$ mm) is considered for the bottom layer while a thicker substrate with a low relative permittivity (Rogers 6006, $\varepsilon_r = 6.15$, $h_1 > h_2$) is used for the top layer. h_1 and h_2 are selected so that the overall height ($h_1 + h_2$) satisfies the resonance condition in the cavity image($Y_{up} + Y_{down} = 0$), where Y_{up} and Y_{down} are described in Eq. (7) and derived based on the network and TL theories, respectively; k_0 is the free-space wavenumber, $n_1 = \sqrt{\varepsilon_{r1}}$, $n_2 = \sqrt{\varepsilon_{r2}}$, Y_0 is air admittance, $\bar{g}$ and $\bar{b}$ are normalized conductance and susceptance of PRS, and h_1 and h_2 are indicated in Fig. 10. Note that a two-port network (characterized by admittance matrix) can describe the thick PRS.[31] This two-port network is terminated with an air admittance (Y_0), as shown in Fig. 10,

$$Y_{down} = jn_1 Y_0 \frac{n_1 - n_2\cot(n_2 k_0 h_2)\cot(n_1 k_0 h_1)}{n_1\cot(n_1 k_0 h_1) + n_2\cot(n_2 k_0 h_2)},$$
$$Y_{up} = Y_{11} - \frac{Y_{12} Y_{21}}{Y_0 + Y_{22}} = Y_0(\bar{g} + j\bar{b}). \qquad (7)$$

By substituting (7) into the transverse resonance condition image($Y_{up} + Y_{down} = 0$), h_1 is evaluated according to (8) and plotted in Fig. 11 for both SMR and MMR PRSs with nominal dimensions shown in Figs 4 and 6, respectively. As shown, h_1 can be estimated around 1.5 mm at 27.5 GHz for both antennas,

$$h_1 = \frac{1}{n_1 k_0}\cot^{-1}\left(\frac{n_1^2 + n_2\cot(n_2 k_0 h_2)\bar{b}}{n_1 n_2\cot(n_2 k_0 h_2) - n_1\bar{b}}\right). \qquad (8)$$

B. Leaky-wave analysis

The well-known transverse resonance technique along with the theory of small reflections[42] is employed to evaluate the leaky-wave attenuation and phase constants in a double-layer cavity. This
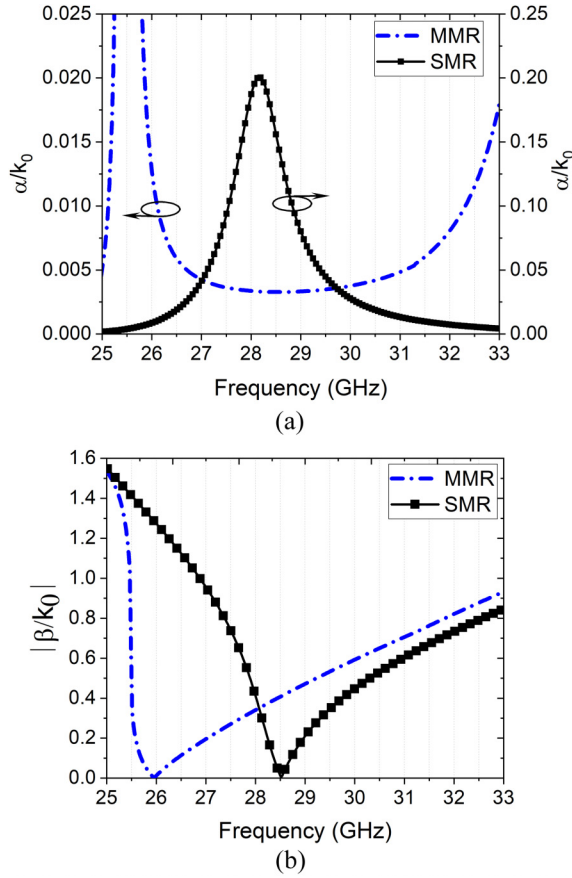
FIG. 12. Leaky-wave (a) attenuation and (b) phase constants of both SMR and MMR antenna.

approximate yet accurate-enough methodology facilitates the calculations in a heterogeneous cavity. In a special case where the ratio of relative permittivity of dielectrics in a double-layer cavity is within the specified range of $0.6 < \varepsilon_{r1}/\varepsilon_{r2} \leq 1$, a set of analytical Eq. (9) can be derived to evaluate the leaky-wave phase and attenuation constants (a derivation is provided in the Appendix). It should be noted that a set of transcendental equations described in the Appendix should be numerically solved for other ratios of dielectric constants. The equations in Eq. (9) are used to obtain the leaky-wave attenuation and phase constants and the results are shown in Fig. 12.

As shown, the MMR-based antenna (antenna with an MMR PRS) not only provides a substantially lower attenuation constant (by a factor of around 35) around the cavity resonance (27.5 GHz) than the SMR counterpart, but also the variations in attenuation constant vs frequency in the MMR-based antenna are much smoother around the cavity resonance. This feature may contribute to an improved broadside directivity since a larger portion of the radiating aperture is involved and contributes to radiation. Furthermore, the phase constant in the MMR antenna around the

cavity resonance is notably less than that in the SMR-based antenna. This provides a smoother phase variation on the antenna's aperture,

$$
\frac{\beta}{k_0} = \sqrt{\frac{-\zeta_1 + \sqrt{\zeta_1^2 + 4\zeta_2^2}}{2k_0\left(\frac{h_1}{n_1} + \frac{h_2}{n_2}\right)}},
$$

$$
\frac{\alpha}{k_0} = \sqrt{\frac{\zeta_1 + \sqrt{\zeta_1^2 + 4\zeta_2^2}}{2k_0\left(\frac{h_1}{n_1} + \frac{h_2}{n_2}\right)}},
$$

$$
\zeta_1 = (\varphi_{PRS} - (2n-1)\pi) - 2k_0(n_1 h_1 + n_2 h_2),
$$

$$
\zeta_2 = Ln\sqrt{|\Gamma_{PRS}|}, \quad n = 0, \pm 1, \pm 2, \pm 3, \ldots
$$

(9)

To validate the analytical results, the calculated leaky-wave attenuation and phase constants (cf. Fig. 12) are employed to calculate Γ_{PRS} and φ_{PRS} by (10) and (11). The longitudinal propagation constant $k_{z1,2} = \beta_{z1,2} + j\alpha_{z1,2}$ (z-axis shown in Fig. 10) in each layer is obtained by using the transverse propagation constant ($k_t = \beta - j\alpha$) in Eq. (10). Then, a system of equations with two unknown parameters (Γ_{PRS}, φ_{PRS}) in Eq. (11) is solved at each frequency to obtain (Γ_{PRS}, φ_{PRS}) (where $\Gamma_0^{TM/TE}$ and $\varphi_{\Gamma_0}^{TM/TE}$ are described in the Appendix, $h_1 = 1.5$ and $h_2 = 0.635$ mm are the thickness of layers in the cavity $k_{LW}^{SMR}/k_0 = \overline{\beta^{SMR}} - j\overline{\alpha^{SMR}} = 0.72 - j0.12$ and $k_{LW}^{MMR}/k_0 = \overline{\beta^{MMR}} - j\overline{\alpha^{MMR}} = 0.31 - j0.003$). It is worth noting that employing either the TE or TM leaky-wave mode leads to the same results, according to the theory of planar leaky-wave antenna.[30–32]

The obtained Γ_{PRS} and φ_{PRS} are compared in Fig. 13 with those evaluated by HFSS for the SMR and MMR PRSs. A good consistency between analytical and full-wave simulation results confirms the accuracy of (9) [the derivations of (10) and (11) are given in the Appendix],

$$
\beta_{z1,2} = \sqrt{\frac{(\alpha^2 - \beta^2 + \varepsilon_{r1,2}k_0^2) + \sqrt{(\alpha^2 - \beta^2 + \varepsilon_{r1,2}k_0^2)^2 + (2\alpha\beta)^2}}{2}},
$$

$$
\alpha_{z1,2} = \sqrt{\frac{-(\alpha^2 - \beta^2 + \varepsilon_{r1,2}k_0^2) + \sqrt{(\alpha^2 - \beta^2 + \varepsilon_{r1,2}k_0^2)^2 + (2\alpha\beta)^2}}{2}},
$$

(10)

$$
\begin{cases}
|\Gamma_0^{TE/TM}|\cos\psi_1 + e^{2h_2\alpha_{z2}}\cos\psi_2 = \dfrac{e^{-2h_1\alpha_{z1}}}{|\Gamma_{PRS}|}, \\
|\Gamma_0^{TE/TM}|\sin\psi_1 + e^{2h_2\alpha_{z2}}\sin\psi_2 = 0,
\end{cases}
$$

$$
\psi_1 = \varphi_{PRS} + \varphi_{\Gamma_0}^{TE/TM} - 2h_1\beta_{z1},
$$

$$
\psi_2 = \varphi_{PRS} + \pi - 2(h_1\beta_{z1} + h_2\beta_{z2}).
$$

(11)

Since the full-wave simulation of a large antenna with double-layer cavity and high-κ substrate involves a large amount of resource and time, an analytical model in Eq. (12)[29,34] is used in
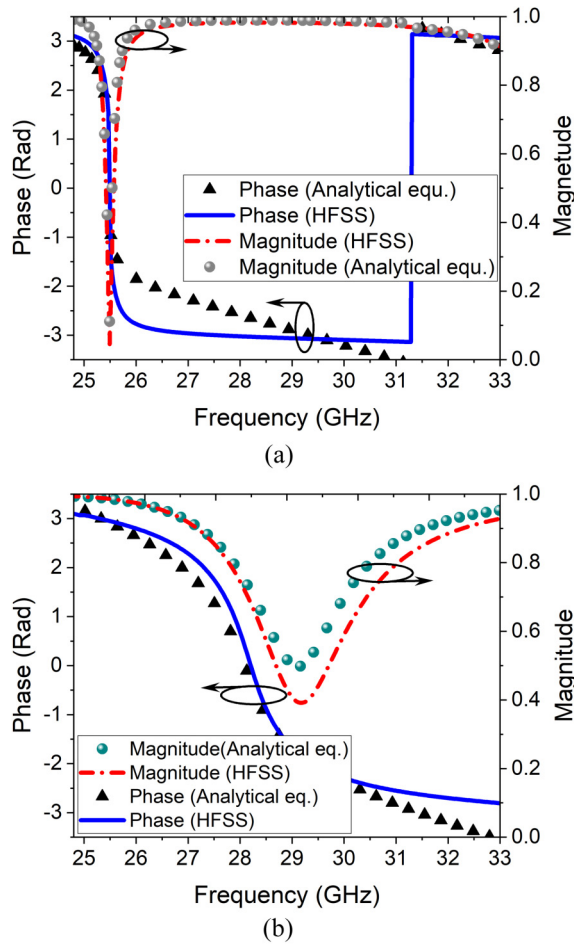
FIG. 13. Magnitude and phase of reflection coefficient evaluated by (10) and (11) and full-wave simulations (HFSS) for both (a) MMR and (b) SMR antenna.
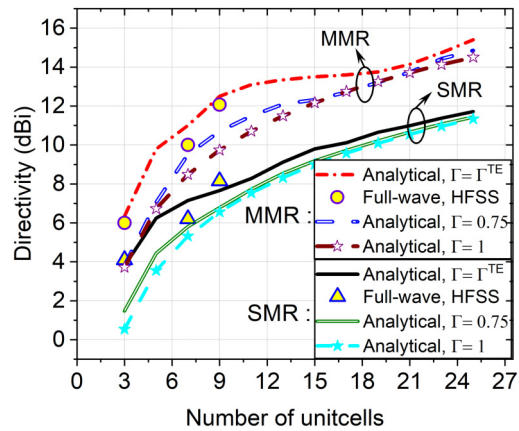

FIG. 14. Evaluated directivity of SMR ($k_{LW}^{SMR}/k_0 = \bar{\beta} - j\bar{\alpha} = 0.72 - j0.12$) and MMR ($k_{LW}^{MMR}/k_0 = \bar{\beta} - j\bar{\alpha} = 0.31 - j0.003$) antennas at 27.5 GHz by (12) with different values of edge reflections ($\Gamma^{edge} = \Gamma^{TE}$, 0.75, 1) and full-wave simulations (HFSS). Full-wave results are comparable to analytical results for $\Gamma^{edge} = \Gamma^{TE}$ in both SMR and MMR PRSs.

this work to estimate broadside directivity for a large radiating aperture.

$$f_{aper.}(np) = e^{-jk_{LW}|np|} + 2\cos(k_{LW}|np|)\left(\frac{\Gamma^{TE/TM}e^{-jk_{LW}L}}{1 - \Gamma^{TE/TM}e^{-jk_{LW}L}}\right),$$

$$F^{f.f.}(\theta) = \cos\theta \sum_{n=-(N-1)/2}^{(N-1)/2} (f_{aper.}(np)e^{jk_0(np)\sin\theta}), \quad (12)$$

$$D(\theta) = \frac{2|F^{f.f.}(\theta)|^2}{\int_0^{\pi/2}|F^{f.f.}(\theta')|^2\sin\theta'd\theta'}.$$

The analytical model is used to evaluate the antenna directivity at broadside ($\theta = 0$ in (12)), for various edge reflection coefficients, with regard to a number of unit cells, as illustrated in Fig. 14, which incorporates the edge reflections of a truncated aperture, where f_{ap} is aperture field, "p" is periodicity, $k_{LW}^{die.} = k_t^{die.} = \beta - j\alpha$, "$L$" is antenna length, $\Gamma^{TE} = (k_t^{die.} - k_t^{air})/(k_t^{die.} + k_t^{air})$ is edge reflection coefficient for TE mode,

$k_t^{air} = \sqrt{k_0^2 - k_z^2}$, $k_z = \sqrt{\varepsilon_r k_0^2 - (k_t^{die.})^2}$, k_0 is free-space wavenumber. Generally, there are noticeable reflections at the antenna's truncated edges that can impact the directivity of the antenna, particularly in the case of an antenna with a lower attenuation constant.

It is worth noting that applying either Γ^{TE} or Γ^{TM} (edge reflection coefficients for TE and TM leaky-wave modes, respectively) which corresponds to the H-plane and E-plane reflection coefficients, respectively results in the same broadside directivity.[31,32] As shown in Fig. 14, there is a significant difference in the directivity of the two antennas, particularly with $N > 6$. Compared to SMR-based antennas in the MMR counterpart, edge reflections have a more noticeable impact on the directivity of the antenna. Edge reflections, however, have a negligible influence on directivity for unitcell numbers more than 18 ($N > 18$), as all corresponding curves in both MMR and SMR antennas are converging together.

The effects of height and permittivity ratio on leaky-wave phase and attenuation constants in the double-layer cavity MMR-based antennas are shown in Fig. 15. In this case, the height and relative permittivity of the first layer, as well as the unit cell geometrical parameters mentioned in Secs. II and III, are assumed to be constant, while the top layer's relative permittivity ε_{r1} and thickness h_1 are swept, and the transverse phase and attenuation constants are calculated by (9). With reference to Fig. 15, using a thicker substrate on the top layer (larger h_1/h_2) with a lower relative permittivity (smaller $\varepsilon_{r1}/\varepsilon_{r2}$) reduces both phase and attenuation constants.

It should be noted that to design an antenna with the desired leaky-wave parameters (α, β) according to Fig. 15, the cavity resonance condition mentioned in Eq. (8) should also be addressed to obtain maximum directivity.
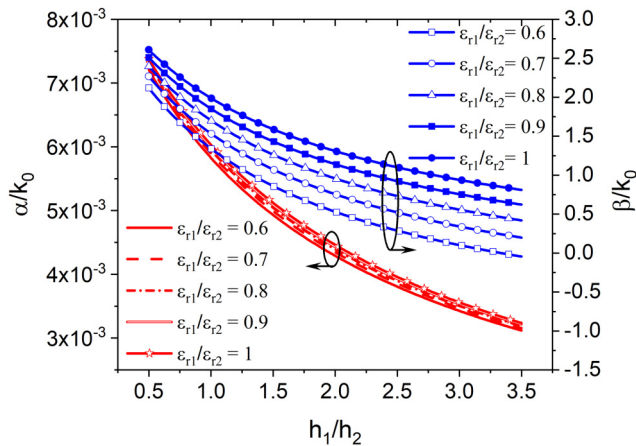
FIG. 15. Variations of leaky-wave attenuation and phase constants in the MMR antenna for different values of relative permittivity ratio with respect to the ratio of substrates' heights in the cavity.

C. Effects of edge's reflection coefficient on directivity

Figure 16 illustrates a heatmap of the antenna's directivity, which is evaluated by (12), for both SMR and MMR PRSs with respect to the magnitude and phase of the edge's reflection coefficient of antenna at the resonant frequency with nominal parameters values and $N = 5$. As described, peak broadside directivity in the SMR antenna corresponds to $\Gamma_{edge} \approx e^{j\pi}$ while it shows a minimum at $\Gamma_{edge} = 1$. Maximum and minimum broadside directivities in the MMR antenna correspond to $\Gamma_{edge} \approx e^{j3.4}$ and $\Gamma_{edge} \approx e^{j4.7}$, respectively.

This figure shows that the antenna directivity is a function of the edge's reflection coefficient. The various edge's reflection coefficients can be realized by different antenna lengths, according to the TL theory. This figure also illustrates that, in comparison to the SMR, the variation of directivity in the MMR-based antenna is significantly greater when considering edge reflections.
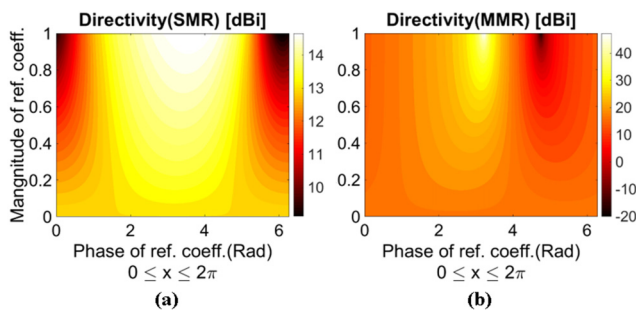

FIG. 16. Heatmap of evaluated antenna's directivity using (12) with respect to magnitude and phase of edge reflection coefficient (Γ^{edge}), for $N = 5$, $f = 27.5$ GHz, (a) SMR PRS with $k_{LW}^{SMR}/k_0 = \bar{\beta} - j\bar{\alpha} = 0.72 - j0.12$, and (b) MMR PRS with $k_{LW}^{MMR}/k_0 = \bar{\beta} - j\bar{\alpha} = 0.31 - j0.003$.

D. Full-wave simulation of developed MMR and SMR antennas

Two 9×9 antennas based on SMR and MMR concept and heterogeneous cavities are developed and analyzed using HFSS in this subsection, and the results are compared. Those two antennas are designed based on a 2-D arrangement of unit cells on Roger RT/duroid 6006 with $\varepsilon_r = 6.15$ on the top layer and Roger RT/duroid 6010 with $\varepsilon_r = 10.2$ on the bottom layer as their geometries are detailed in Fig. 17. Each antenna's cavity is fed through an opening etched in the ground plane and excited by a wave port in HFSS. In both antennas, the bottom layer (Roger RT/duroid 6010) beyond the cavity area is covered by a metallic sheet (copper cladding) and surrounded by SIW-like metallic walls to eliminate the adverse effects of edge diffractions on radiation patterns caused by surface wave propagation on the bottom substrate. These metallic walls (SIW-like walls) also inhibit the propagation and diffraction of excited parallel-plate waveguide (PPWG) mode in the bottom layer. It is worth noting that in Fig. 17(b), the center unitcell's dimensions in the top layer have been modified by about 25% to improve impedance matching at the waveport.

Full-wave simulations are used to evaluate antenna realized gain and directivity at broadside, and the results are shown in Fig. 18. The peak directivity of the MMR and SMR antennas are located at approximately 27.37 and 27.19 GHz, respectively with slight offsets from 27.5 GHz. Obviously, an MMR antenna shows an appreciable improvement in broadside gain and directivity by more than 4 dBi compared to that of an SMR antenna. The peak directivity for MMR antenna in Fig. 18(b) is 16.1 corresponding to 12.07 dBi which agrees well with 12.25 dBi evaluated analytically in Fig. 14 with $N = 9$ and $\Gamma^{edge} = \Gamma^{TE}$. The peak directivity of the SMR antenna is estimated as 7.5 dBi analytically, while this value is 8.15 dBi in a full-wave simulation.

According to Fig. 18(a), the 3 dB pattern bandwidth in the MMR antenna is around 3.3% (26.75–27.65 GHz), while the SMR antenna shows only 1.65% pattern bandwidth (27.1–27.55 GHz). The 1.65% improvement in the pattern bandwidth of the MMR antenna is attributed to a smooth variation of the phase of the reflection coefficient around the cavity resonance at 27.5 GHz in Fig. 13(a). Figure 19 compares the E-plane and H-plane radiation patterns (directivity) of SMR and MMR antennas. As illustrated, the radiation pattern of the antenna utilizing MMR PRS improves noticeably as compared to the SMR PRS.

With reference to Fig. 12(b) at peak directivity, in comparison to SMR antenna with $\beta/k_0 = 0.72$, the MMR antenna with $\beta/k_0 = 0.31$ provides a more uniform phase distribution throughout the antenna aperture. Furthermore, in the SMR antenna $\alpha/k_0 = 0.072$, whereas this value is around $\alpha/k_0 = 0.003$ for the MMR antenna. These analyses suggest that the antenna with MMR PRS should be able to provide greater control over the attenuation constant as well as a smoother phase fluctuation in the radiating aperture, thus leading to improved radiation behavior.

A further investigation shows that the aperture field intensity is reduced at the antenna's edges by a factor of $E(L/2)/E_0 \approx \exp(-\alpha L/2)$, where E_0 is field intensity at the antenna's center, L is antenna's length, and α is the attenuation constant. Using nominal values for "α" and "L" ("W_P" in Fig. 17) in both
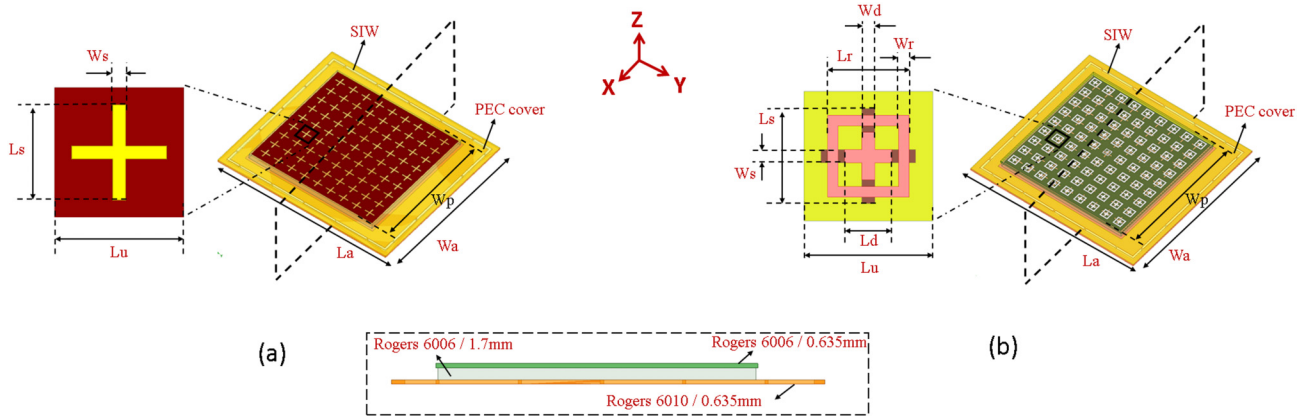
FIG. 17. 3-D and cross sectional views of two 9 × 9 antennas along with corresponding unit cells with (a) SMR antenna, Lu = 4.9, Ls = 3.6, Ws = 0.5, Wp = 46.4, Wa = 60, La = 63.25 and (b) MMR antenna, Ls = 3.6, Ws = 0.4, Wp = 46.4, Wa = 60, La = 63.25, Lr = 3.1, Wr = 0.4, Ld = 1.8, Wd = 0.5, Lu = 4.9 (all dimensions are in millimeters). In both antennas, the YoZ plane is the E-plane and the XoZ plane is the H-plane.
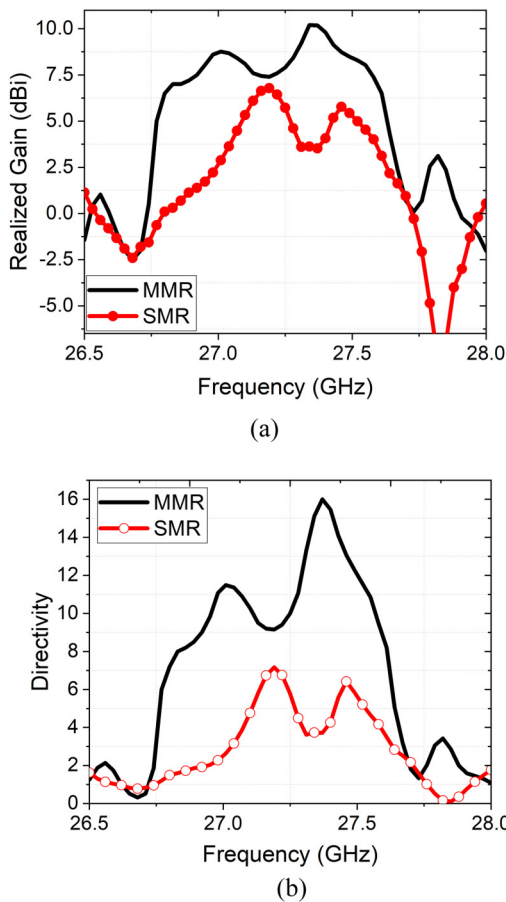
SMR and MMR antennas reveals that in the SMR antenna, only 4% of power meets the edges while this value is 91% for the MMR antenna. It turns out that in the SMR antenna, 90% of the power is radiated within 70% of the antenna's aperture. Therefore, the

FIG. 18. Simulated broadside (a) gain and (b) directivity of both MMR and SMR antennas as shown in Fig. 17.
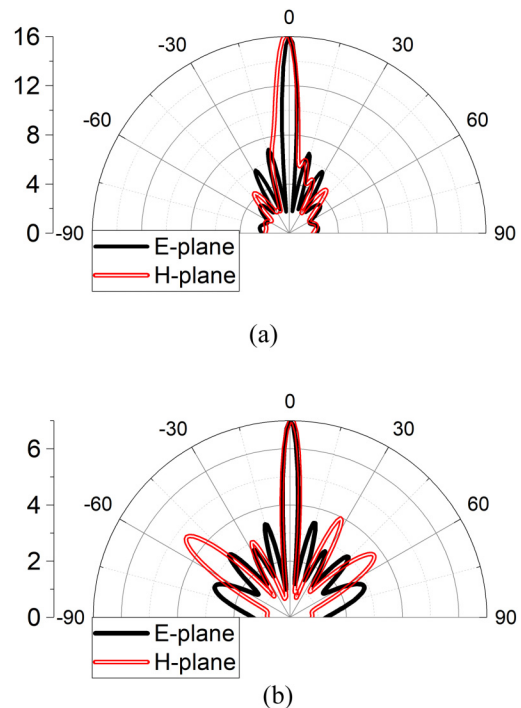

FIG. 19. Simulated radiation pattern (directivity) of (a) MMR antenna [cf. Figure 17(b)] and (b) SMR antenna [cf. Figure 17(a)] in both principal planes.
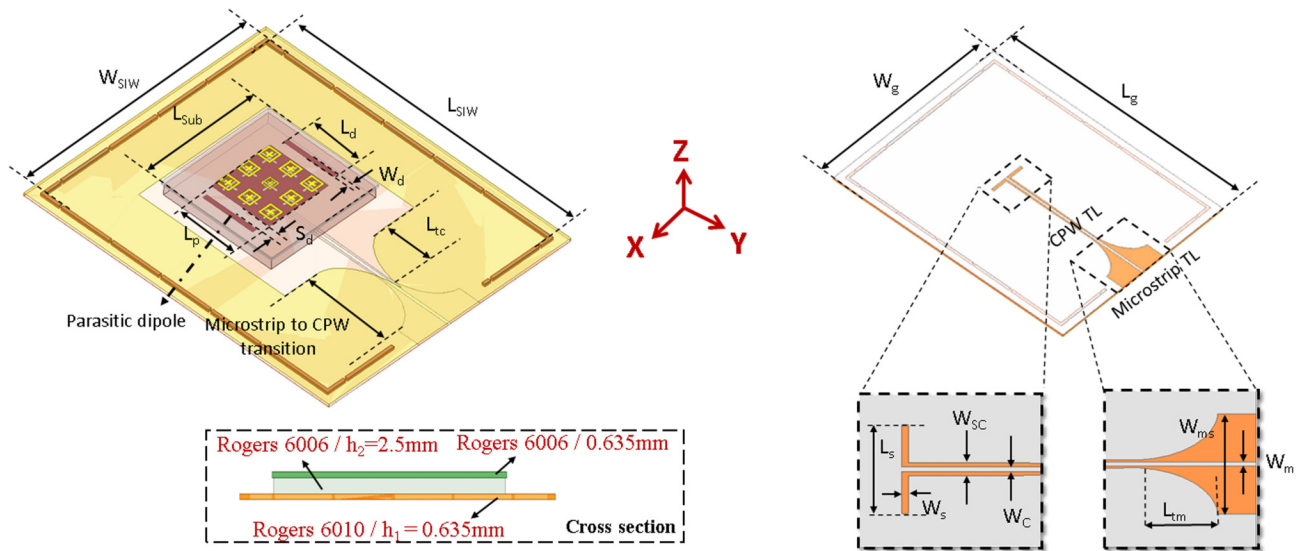
FIG. 20. 3-D and cross section views of the proposed dual-band antenna with MMR PRS along with corresponding dimensions (in millimeters): W_{SIW} = 69.2, L_{SIW} = 56, L_d = 12, W_d = 1, S_d = 2.15, L_p = 14, L_{Sub} = 26.5, L_{tc} = 12, L_s = 11, W_s = 0.8, W_{sc} = 1.6, W_c = 0.6, L_{tm} = 10.35, W_{ms} = 15.2, W_m = 0.6.

antenna surface that effectively contributes to the radiation in the MMR antenna is found to be larger than that in the SMR antenna.

V. DUAL-BAND ANTENNA WITH A LARGE FREQUENCY RATIO

The developed and studied MMR-based antenna is used in this section to propose a single-fed dual-band antenna with a double-layer cavity that operates at both S-band (3.2 GHz) and Ka-band (27.5 GHz) for highly integrated ARoF applications. The measurement results are then presented to validate the full-wave simulation results.

Figures 20 and 21 illustrate the 3D geometry of the proposed dual-band antenna and the fabricated prototype, respectively. The

FIG. 21. Top and bottom views of the fabricated proposed dual-band antenna.

overall structure consists of three stacked layers, which are glued and then pressed under high pressure to form a uniform connection, according to the PCB fabrication process in our Poly-Grames Research Center. The bottom layer (feeding line layer) is Rogers RT/duroid 6010 with $\varepsilon_r = 10.2$ and 25 mil thickness. The middle layer and top layer are Rogers RT/duroid 6006 with $\varepsilon_r = 6.15$ and a standard thickness of 100 and 25 mil. The antenna is fed by a CPW transmission line (CPW TL) terminated at the radiating aperture's center by a transverse slot etched on the ground plane.

In the Ka-band, the antenna radiates as a 3×3 leaky-wave surface, while in the S-band, the antenna operates as a large square patch antenna excited by an etched slot on the ground plane, forming an aperture-coupled antenna. To accommodate an end-launch connector for our measurement purposes, a transition from an ungrounded CPW TL to a microstrip line is designed to provide a proper impedance matching condition in both frequency bands.

The main architecture and substrates used in this antenna are the same as in Fig. 17(b), but this antenna is driven by a CPW TL. Because of the parasitic effects of CPW TL within the cavity, a thicker substrate is required in the middle layer compared to Fig. 17(b) to obtain maximum directivity at 27.5 GHz. The top surface of the bottom layer (feeder layer) is covered by a metallic sheet and surrounded by a SIW-like wall to prevent the excitation and propagation of SW and PPWG modes. The operation of the antenna in each frequency band is outlined in Subsections V A and V B.

A. Radiation in S-band

Since the antenna radiates like an aperture-coupled patch antenna in this frequency range, the E-plane length (along the y-axis in Fig. 20) is adjusted to be roughly a half of the guided
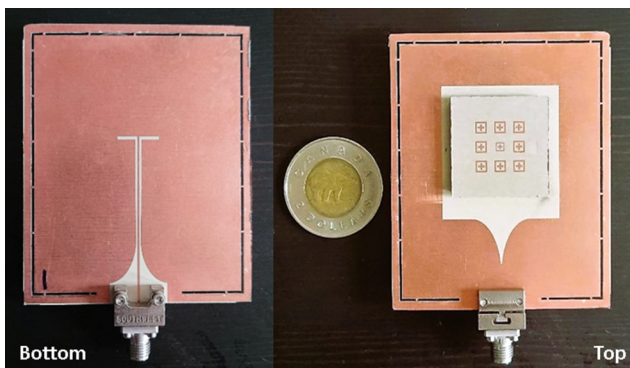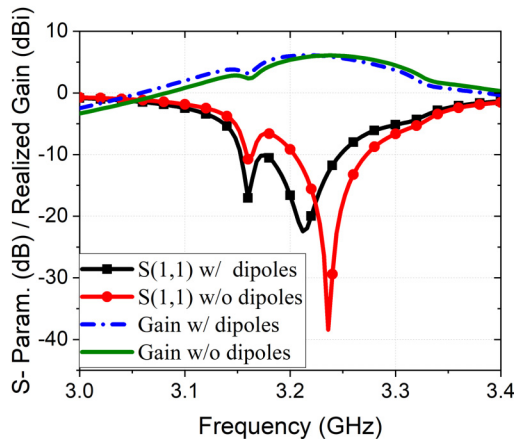
FIG. 22. Effects of parasitic dipoles on reflection coefficient and realized gain of the dual-band antenna in the S-band.

FIG. 23. Effects of SIW-like walls around the antenna on reflection coefficient in the S-band without (w/o) SIW wall, with (w/) SIW wall, and with SIW wall with an additional 10 mm offset in each direction.

wavelength $\lambda_0^L/2\sqrt{\varepsilon_{r1}}$, where λ_0^L is free-space wavelength at the lower resonance frequency (3.2 GHz) and $\varepsilon_{r1} = 6.15$.

The aperture width (length in the H-plane direction, along the x-axis) is also tuned to achieve the optimum impedance matching. The overall dielectric thickness ($h = h_1 + h_2$ in Fig. 20) should be in the range of $0.01 < h/\lambda_g^L < 0.11$[43] to ensure the antenna can radiate properly as a patch antenna. Note that, since the antenna should operate simultaneously in both frequency bands, all dimensions should be optimized to achieve the best possible results in both frequency bands.

Two parasitic dipoles (shown in Fig. 20) on both sides of the radiating aperture in the middle layer improve the impedance matching by properly coupling to the antenna as illustrated in Fig. 22. The length of the parasitic dipoles is initially set around $\lambda_0^L/2\sqrt{\varepsilon_{r1}}$ to excite the fundamental mode of surface current. The dimensions of the dipoles and their distance from the antenna are optimized to achieve the best possible results in both bands. The optimization procedures are not discussed in this work for the sake of brevity.

Effects of the surrounded metallic walls are also studied in Fig. 23, indicating its tangible effects on the impedance bandwidth of the antenna. Simulated and measured reflection coefficients and radiation patterns in both principal planes are compared in Figs. 24 and 25, respectively, which indicates a reasonable consistency between the measurement and simulation results. Simulated and measured peak gains realized in this work are around 6 and 5.62 dBi, respectively. The asymmetry observed in the measured pattern along the E-plane is attributable to diffractions from the end-launch connector during measurements. Cross polarization levels are better than -30 dBi in both principal planes.

B. Radiation in Ka-band

As indicated briefly earlier, the antenna in this frequency band radiates as a leaky-wave surface, as discussed in Sec. IV D. According to Sec. V A, the antenna length (length along the y-axis)
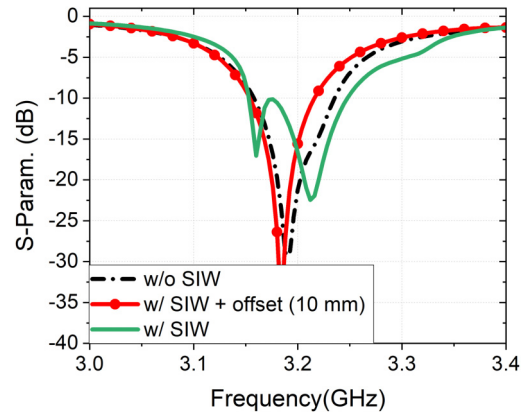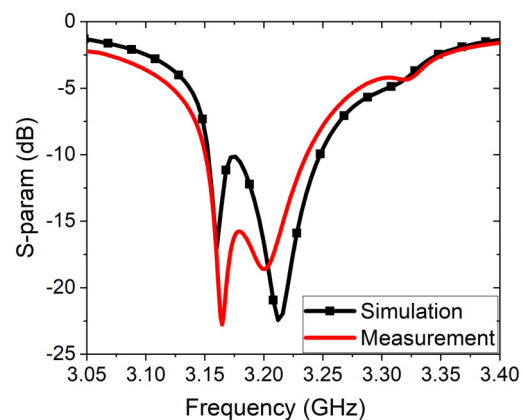

FIG. 24. Simulated and measured reflection coefficients of the proposed dual-band antenna in the S-band.

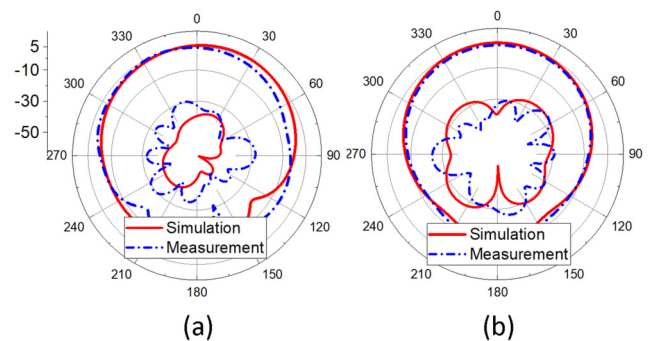**FIG. 25.** Simulated and measured (a) E-plane and (b) H-plane radiation patterns of the proposed dual-band antenna in the S-band.
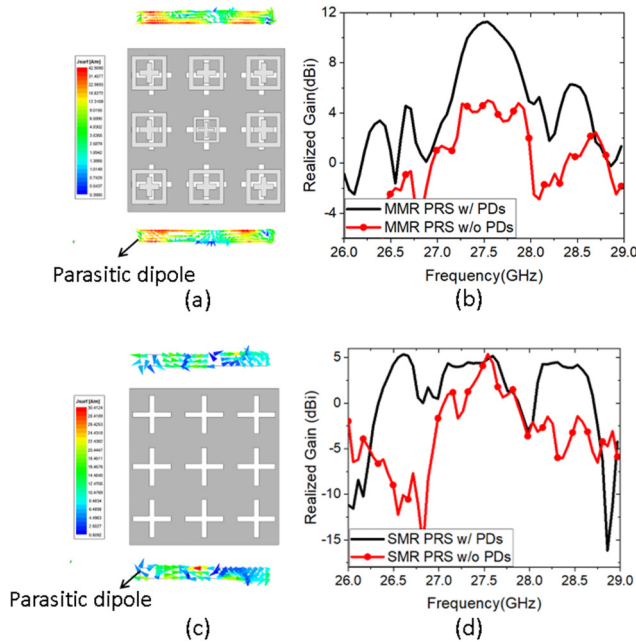
FIG. 26. Current distribution on parasitic dipoles along with simulated realized gain with (w/) and without (w/o) parasitic dipoles in the proposed dual-band antenna with (a) and (b) MMR PRS, and (c) and (d) SMR PRS.

is initially adjusted around $\lambda_0^L/2\sqrt{\varepsilon_{r1}}$ and, subsequently, optimized using a full-wave simulation. The number of unit cells is determined as follows. In the upper-frequency band (Ka-band), the antenna should operate in a "no grating lobe regime,"[29] therefore, the unit-cell dimension (i.e., periodicity) should be turned around a half of free-space wavelength in the upper-frequency band. Therefore, the number of unit-cell is calculated as

$$\lambda_0^L/\left(2\sqrt{\varepsilon_{r1}}\right) = N(\,\lambda_0^H/2),$$
$$N = \lambda_0^L/\lambda_0^H\sqrt{\varepsilon_{r1}}. \tag{13}$$

Considering $f_0^L = 3.2$ GHz, $f_0^H = 27.5$ GHz, and $\varepsilon_{r1} = 6.15$, the number of unit cells in each principal plane is $N = 3$. With reference to Fig. 14, peak directivity with $N = 3$ and $\Gamma^{edge} = \Gamma^{TE}$ is expected to be around 6 dBi for an MMR antenna and around 3.8 dBi for an SMR antenna.

The optimized dimensions of two parasitic dipoles are around $2.7\lambda_0^H/\sqrt{\varepsilon_{r1}}$ in the Ka-band. As such, a higher order mode of surface currents [see Figs. 26(a) and 26(c)] are induced on the parasitic dipoles at 27.5 GHz. In-phase induced currents across the dipoles, as shown in Fig. 26(a), act as a two-element in-phase antenna array, creating coherent radiations at the broadside. However, in the SMR antenna, substantially smaller surface currents are induced on the dipoles, revealing a weaker coupling between the dipoles and leaky-waves at the aperture edges [see Fig. 26(c)]. This is explained by the leaky-wave analysis shown in Fig. 12(a).
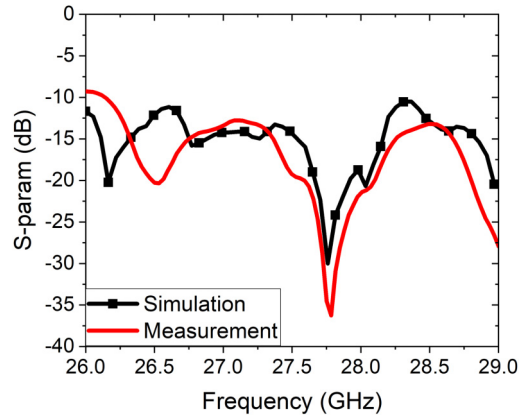

FIG. 27. Simulated and measured reflection coefficients of the proposed dual-band antenna in the Ka-band.

An SMR antenna has a substantially higher leaky wave attenuation constant at 27.5 GHz than an MMR antenna. As a result, in the MMR antenna, weakly attenuated leaky-waves reach the antenna edges, where they induce stronger surface current on the dipoles, resulting in a significant improvement in antenna gain. In the SMR antenna, dipole contributions to radiation are negligible due to weakly induced surface currents on the parasitic dipoles. Figures 26(b) and 26(d) illustrate the gain profile vs frequency with and without parasitic dipoles for both MMR- and SMR-based antennas, respectively. Because of the minimal coupling between the dipoles and leaky-waves at the edges in the SMR-based antenna, its gain is only increased by around 0.5 dBi, from 4.5 to roughly 5 dBi.

The gain in the MMR, on the other hand, is roughly 5.8 dBi without dipoles and increased up to 11.75 dBi with parasitic dipoles indicating around 6 dBi improvement. The MMR-based antenna's aperture efficiencies without and with parasitic dipoles are around 14% and 43%, respectively. Simulated and measured reflection coefficients and normalized radiation patterns in both principal planes are compared in Figs. 27 and 28, respectively. Reasonable consistencies are observed between simulation and
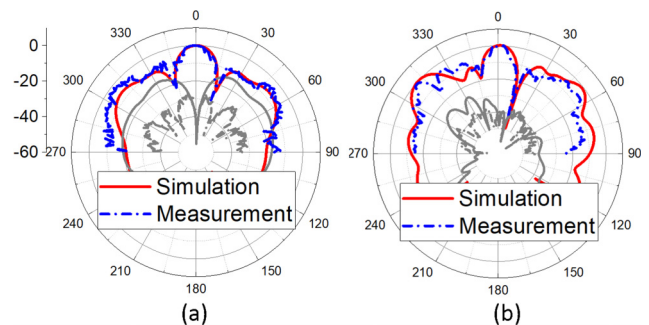

FIG. 28. Simulated and measured (a) E-plane and (b) H-plane radiation patterns of the proposed dual-band antenna in the Ka-band.

measurement results. Simulated and measured cross polarization levels in the radiation pattern are better than −18 dBi in both principal planes, while the measured co-polarization level (realized gain) is around 9.6 dBi at the broadside.

With reference to Fig. 28, the H-plane pattern has a relatively high side lobe level (SLL), which could be attributed to the following effects: (1) parasitic radiation of excited higher order modes in the discontinuity between CPW and slot; (2) parasitic CPW TL radiation inside the cavity and parasitic radiation from the transition between CPW TL and microstrip line, and; (3) radiation from higher-order modes of surface currents induced on the parasitic dipoles, which positively contribute to the antenna's radiation at a particular spatial angle.

VI. CONCLUSIONS

We investigated the effects of increasing the relative permittivity of the substrate on radiation performance in a substrate-integrated planar leaky-wave antenna with SMR PRS for the first time. We showed that the cavity and PRS resonances tend to merge as relative permittivity is raised. According to the analytical studies and full-wave simulations in this scenario, the magnitude of the PRS's reflection coefficient on a high-κ substrate is significantly reduced, which means a transparent PRS, causing a directivity loss at the broadside. We proved how adopting an MMR PRS can successfully handle this issue and result in a significant improvement in the antenna broadside directivity and radiation pattern. According to our studies, an MMR PRS is set to provide a larger PRS susceptance with a smooth variation over a specified frequency range. Additionally, it has a lower leaky-wave attenuation constant, thus enhancing the broadside radiations in accordance with the planar leaky-wave theory. A set of analytical equations for leaky-wave analysis of the antenna designed on a heterogeneous material were developed using the theory of small reflections. The results were confirmed by full-wave simulations.

Finally, we developed, evaluated, and fabricated a class of single-fed dual-band antennas with a heterogeneous cavity that radiates in both S-band and Ka-band to shed light on the development of an integrated antenna-frontend in an ARoF system.

APPENDIX: ANALYSIS OF HETEROGENEOUS CAVITY

Leaky-wave analysis of the double-layer cavity

In Fig. 29, the transverse resonance technique in the form of a reflection coefficient is used to calculate the transverse propagation constant in a double-layer cavity at $Z = 0$ (reference line) according to (A1), where $\Gamma_{PRS} = |\Gamma_{PRS}|e^{j\varphi_{PRS}}$ is the upward reflection coefficient at reference line (or PRS reflection coefficient at $Z = 0^-$); Γ_{REF} is the downward reflection coefficient at
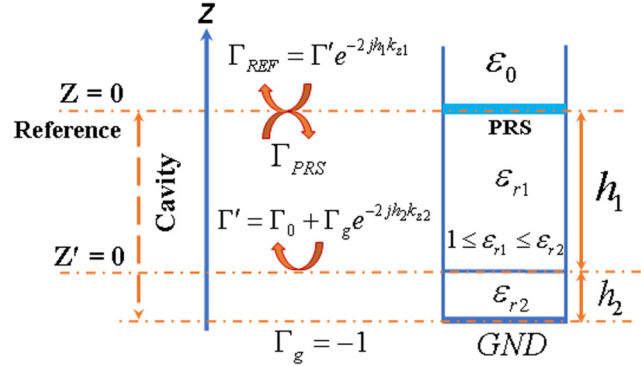

FIG. 29. TL model of the leaky-wave antenna with a double-layer cavity.

the reference line (or equivalently reflection coefficient at $Z = 0^+$),

$$\Gamma_{PRS}\Gamma_{REF} = 1. \tag{A1}$$

According to the TL theory $\Gamma_{REF} = \Gamma' e^{-2jh_1k_{z1}}$, where Γ' is the reflection coefficient evaluated at $Z' = 0^+$. Therefore,

$$\Gamma_{PRS}\Gamma' e^{-2jh_1k_{z1}} = 1. \tag{A2}$$

At the boundary of two dielectrics, an infinite number of reflections takes place. However, according to the theory of small reflections,[42] the overall reflection coefficient at the $Z' = 0$ boundary [Γ' in Eq. (A3)] can be approximated as a combination of two terms including the reflection coefficient between two dielectrics ($\Gamma_0^{TE/TM}$) as described in Eq. (A3) and reflection coefficient of the ground plane transferred to $Z' = 0$ boundary ($\Gamma_g e^{-2jh_2k_{z2}}$), where $\Gamma_g = -1$ is the reflection coefficient of the ground plane,

$$\Gamma' \approx \Gamma_0^{TE/TM} + \Gamma_g e^{-2jh_2k_{z2}}, \tag{A3}$$

$$\Gamma_0^{TE/TM} = |\Gamma_0^{TE/TM}|e^{j\varphi_{\Gamma_0}^{TE/TM}}$$

$$= \begin{cases} \Gamma_0^{TE} = \dfrac{Z_2^{TE} - Z_1^{TE}}{Z_2^{TE} + Z_1^{TE}} = \dfrac{k_{z1} - k_{z2}}{k_{z1} + k_{z2}} \\[3mm] \Gamma_0^{TM} = \dfrac{Z_2^{TM} - Z_1^{TM}}{Z_2^{TM} + Z_1^{TM}} = \dfrac{\varepsilon_{r1}k_{z2} - \varepsilon_{r2}k_{z1}}{\varepsilon_{r1}k_{z2} + \varepsilon_{r2}k_{z1}} \end{cases}.$$

Substituting (A3) into (A2), a system of equations can be developed according to (A4),

$$\begin{cases} |\Gamma_0^{TE/TM}|\cos\psi_1 + e^{2h_2\alpha_{z2}}\cos\psi_2 = \dfrac{e^{-2h_1\alpha_{z1}}}{|\Gamma_{PRS}|}, \\[3mm] |\Gamma_0^{TE/TM}|\sin\psi_1 + e^{2h_2\alpha_{z2}}\sin\psi_2 = 0, \\[2mm] \psi_1 = \varphi_{PRS} + \varphi_{\Gamma_0}^{TE/TM} - 2h_1\beta_{z1}, \\[2mm] \psi_2 = \varphi_{PRS} + \pi - 2(h_1\beta_{z1} + h_2\beta_{z2}). \end{cases} \tag{A4}$$

where $|\Gamma_{PRS}|$, φ_{PRS} are calculated by a full-wave simulation in an unit-cell; $|\Gamma_0^{TE/TM}|$ and $\varphi_{\Gamma_0}^{TE/TM}$ are described in Eq. (A3); h_1 and h_2 are indicated in Fig. 29; α_{z1}, α_{z2}, β_{z1}, β_{z2} are longitudinal attenuation and phase constants ($k_{z1,2} = \beta_{z1,2} + j\alpha_{z1,2}$; Note that positive sign is selected to realize improper leaky-wave in $e^{-2jh_{1,2}k_{z1,2}}$ terms) in the dielectric 1 and 2, respectively, which can be expressed as a function of transverse propagation constant ($k_t = \beta - j\alpha$) according to (A5) by solving $k_{z1,2} = \beta_{z1,2} + j\alpha_{z1,2} = \sqrt{\varepsilon_{r1,2}k_0^2 - k_t^2}$,

$$\beta_{z1,2} = \sqrt{\frac{(\alpha^2 - \beta^2 + \varepsilon_{r1,2}k_0^2) + \sqrt{(\alpha^2 - \beta^2 + \varepsilon_{r1,2}k_0^2)^2 + (2\alpha\beta)^2}}{2}},$$

$$\alpha_{z1,2} = \sqrt{\frac{-(\alpha^2 - \beta^2 + \varepsilon_{r1,2}k_0^2) + \sqrt{(\alpha^2 - \beta^2 + \varepsilon_{r1,2}k_0^2)^2 + (2\alpha\beta)^2}}{2}}. \quad (A5)$$

Equation (A4) together with (A5) can be numerically solved for finding transverse phase (β) and attenuation (α) constants at each frequency. It is worth mentioning that in an antenna $\alpha/k_0 \ll 1$ and $\beta/k_0 \ll 1$, the binomial approximation $(x + \Delta x)^n \approx x^n + nx^{n-1}\Delta x + \sigma(n-2)$ can be applied to simplify (A5)[44] and approximated it with (A6) where $n_{1,2} = \sqrt{\varepsilon_{r1,2}}$,

$$\beta_{z1,2} \approx \frac{\alpha^2 - \beta^2 + 2n_{1,2}^2 k_0^2}{2n_{1,2}k_0},$$

$$\alpha_{z1,2} \approx \left|\frac{\alpha\beta}{n_{1,2}k_0}\right|. \quad (A6)$$

As mentioned in Sec. IV B, for a specific range of relative permittivity ratios ($0.6 < \varepsilon_{r1}/\varepsilon_{r2} \leq 1$), an analytical equation can be developed for calculating the transverse propagation constant. Since in an antenna with $\alpha/k_0 \ll 1$ and $\beta/k_0 \ll 1$, and particularly, in a high permittivity dielectric, $|k_t/k_0| \ll \varepsilon_{r1,2}$; therefore, $\varepsilon_{r1,2} - (k_t/k_0)^2 = (k_{z1,2}/k_0)^2$ can be approximated as $\varepsilon_{r1,2} \approx (k_{z1,2}/k_0)^2$ in Eq. (A3) and in this case, $|\Gamma_0^{TE/TM}| \approx |\Gamma_0^{TEM}|$.

For $0.6 < \varepsilon_{r1}/\varepsilon_{r2} \leq 1$, $|\Gamma_0^{TE/TM}| < 0.1$; therefore, wave reflection (due to a step change in relative permittivity) between two dielectrics is negligible. In this case, $|\Gamma_0^{TE/TM}|$ can be ignored in Eq. (A4); therefore, $\Gamma' \approx -e^{-2jh_2k_{z2}}$. By considering $|\Gamma_0^{TE/TM}| = 0$ in Eq. (A4) and rearranging it, we can develop (A7) as follows:

$$\begin{cases} \varphi_{PRS} \approx (2n-1)\pi + 2(\beta_{z1}h_1 + \beta_{z2}h_2), \\ |\Gamma_{PRS}| \approx e^{-2(\alpha_{z1}h_1 + \alpha_{z2}h_2)}. \end{cases} \quad (A7)$$

Having substituted (A6) into (A7) and applying some basic algebraic manipulations, the transverse phase and attenuation constants are calculated according to (A8),

$$\frac{\beta}{k_0} = \sqrt{\frac{-\zeta_1 + \sqrt{\zeta_1^2 + 4\zeta_2^2}}{2k_0\left(\frac{h_1}{n_1} + \frac{h_2}{n_2}\right)}},$$

$$\frac{\alpha}{k_0} = \sqrt{\frac{\zeta_1 + \sqrt{\zeta_1^2 + 4\zeta_2^2}}{2k_0\left(\frac{h_1}{n_1} + \frac{h_2}{n_2}\right)}}, \quad (A8)$$

$$\zeta_1 = (\varphi_{PRS} - (2n-1)\pi) - 2k_0(n_1h_1 + n_2h_2),$$

$$\zeta_2 = Ln\sqrt{|\Gamma_{PRS}|}, \quad n = 0, \pm 1, \pm 2, \pm 3, \ldots.$$

A periodic leaky-wave antenna radiates based on the space harmonics (particularly, $n = -1$).[29] In this case, the phase constant of the radiated wave (a fast wave) is described as follows:

$$\beta_n^{rad}/k_0 = \beta_0^{unp.}/k_0 + 2n\pi/pk_0,$$

$$n = -1, -2, -3, \ldots, \quad (A9)$$

where $\beta_0^{unp.}/k_0$ is the normalized phase constant of the unperturbed wave (slow wave) (A8) and "p" is periodicity in the PRS.

AUTHOR DECLARATIONS
Conflict of Interest

The authors have no conflicts to disclose.

Author Contributions

Amirhossein Askarian: Conceptualization (equal); Data curation (equal); Formal analysis (equal); Investigation (lead); Methodology (lead); Project administration (lead); Resources (lead); Software (lead); Supervision (lead); Validation (lead); Visualization (lead); Writing – original draft (lead); Writing – review & editing (equal). **Jianping Yao:** Supervision (supporting); Validation (supporting); Writing – review & editing (equal). **Zhenguo Lu:** Conceptualization (supporting); Funding acquisition (supporting); Supervision (supporting); Validation (supporting); Writing – review & editing (equal). **Ke Wu:** Conceptualization (supporting); Formal analysis (supporting); Funding acquisition (lead); Investigation (equal); Methodology (supporting); Project administration (equal); Resources (lead); Supervision (equal); Validation (equal); Visualization (equal); Writing – review & editing (lead).

DATA AVAILABILITY

The data that support the findings in this study are available from the corresponding author upon reasonable request.

REFERENCES

[1]W. I. Way, "Subcarrier multiplexed light wave system design considerations for subscriber loop applications," J. Lightwave Technol. **7**(11), 1806–1818 (1989).
[2]H. Ogawa, D. Polifko, and S. Banba, "Millimeter-wave fiber optics systems for personal radio communication," IEEE Trans. Microw. Theory Tech. **40**(12), 2285–2293 (1992).

[3]E. S. Lima, R. M. Borges, L. A. Melo Pereira, H. R. Dias Filgueiras, A. M. Alberti, and A. Cerqueira Sodré, "Multiband and photonically amplified fiber-wireless Xhaul," IEEE Access **8**, 44381–44390 (2020).

[4]D. Marpaung, J. Yao, and J. Capmany, "Integrated microwave photonics," Nat. Photonics **13**, 80–90 (2019).

[5]J. Yao, "Photonics for ultrawideband communications," IEEE Microw. Mag. **10**(4), 82–95 (2009).

[6]J. Yao, F. Zeng, and Q. Wang, "Photonic generation of ultrawideband signals," J. Lightwave Technol. **25**(11), 3219–3235 (2007).

[7]K. Zeb, Z. Lu, J. Liu, Y. Mao, G. Liu, P. Poole, M. Rahim, G. Pakulski, P. Barrios, W. Jiang, and X. Zhang, "Inas/InP quantum dash buried heterostructure mode-locked laser for high capacity fiber-wireless integrated 5G new radio fronthaul systems," Opt. Express **29**(11), 16164–16174 (2021).

[8]A. Askarian and K. Wu, "Shared-aperture enabled integration of sub-6 GHz and millimeter-wave antennas for future multi-functional wireless systems," in *2020 IEEE International Symposium on Antenna and Propagation and North American Radio Science Meeting* (IEEE, 2020), pp, 1775––1776.

[9]A. Askarian and K. Wu, "Miniaturized dual-band slot antenna with self-scalable pattern for array applications," in *2020 IEEE International Symposium on Antenna and Propagation and North American Radio Science Meeting* (IEEE, 2020), pp. 1943–1944.

[10]J. F. Zhang, Y. J. Cheng, Y. R. Ding, and C. X. Bai, "A dual-band shared-aperture antenna with large frequency ratio, high aperture reuse efficiency, and high channel isolation," IEEE Trans. Antenn. Propag. **67**(2), 853–860 (2019).

[11]B. J. Xiang, S. Y. Zheng, H. Wong, Y. M. Pan, K. X. Wang, and M. H. Xia, "A flexible dual-band antenna with large frequency ratio and different radiation properties over the Two bands," IEEE Trans. Antenn. Propag. **66**(2), 657–667 (2018).

[12]X. Yang *et al.*, "An integrated Tri-band antenna system with large frequency ratio for WLAN and WiGig applications," IEEE Trans. Ind. Electron. **68**(5), 4529–4540 (2021).

[13]J. Zhu, Y. Yang, S. Liao, and Q. Xue, "Aperture-shared millimeter-wave/Sub-6 GHz dual-band antenna hybridizing Fabry–Perot cavity and Fresnel zone plate," IEEE Trans. Antenn. Propag. **69**(12), 8170–8181 (2021).

[14]Z:-X Xia, K. W. Leung, N. Yang, and K. Lu, "Compact dual-frequency antenna array with large frequency ratio," IEEE Trans. Antenn. Propag. **69**(4), 2031–2040 (2021).

[15]J.-X Chen, S.-H. Cao, and X.-F. Zhang, "SPPs-shared dual-band antenna with large frequency ratio," IEEE Access **8**, 29132–29139 (2020).

[16]A. Askarian, J. Yao, Z. Lu, and K. Wu, "Surface-wave control technique for mutual coupling mitigation in array antenna," IEEE Microw. Wirel. Compon. Lett. **32**(6), 623–626 (2022).

[17]J. B. Keller and F. C. Karal, "Surface wave excitation and propagation," J. Appl. Phys. **31**, 1039 (1960).

[18]J. P. Doane, K. Sertel, and J. L. Volakis, "Matching bandwidth limits for arrays backed by a conducting ground plane," IEEE Trans. Antenn. Propag. **61**(5), 2511–2518 (2013).

[19]G. Goubau, "Surface waves and their application to transmission lines," J. Appl. Phys. **21**, 1119 (1950).

[20]S. S. Attwood, "Surface-wave propagation over a coated plane conductor," J. Appl. Phys. **22**, 504 (1951).

[21]H. S. Tuan, "Scattering of a TM surface wave at a guide deformation," J. Appl. Phys. **44**, 5522 (1973).

[22]L. Li, Q. Chen, Q. Yuan, C. Liang, and K. Sawaya, "Surface-wave suppression band gap and plane-wave reflection phase band of mushroom like photonic band gap structures," J. Appl. Phys. **103**, 023513 (2008).

[23]B. I. Wu, H. Chen, J. A. Kong, and T. M. Grzegorczyk, "Surface wave suppression in antenna systems using magnetic metamaterial," J. Appl. Phys. **101**, 114913 (2007).

[24]J.-W. Jeong and J.-S. Park, "A microcontroller unit-based electromagnetic bandgap control scheme: Application for enhancing isolation in an antenna array and the EMI scanner system speed thereof," IEEE Trans. Microw. Theory Tech. **68**(11), 4536–4553 (2020).

[25]K. Sengupta and A. Hajimiri, "Designing optimal surface currents for efficient On-chip Mm-wave radiators with active circuitry," IEEE Trans. Microw. Theory Tech. **64**(7), 1976–1988 (2016).

[26]S. D. Rogers, "Electromagnetic-bandgap layers for broad-band suppression of TEM modes in power planes," IEEE Trans. Microw. Theory Tech. **53**(8), 2495–2505 (2005).

[27]J. Park, A. C. W. Lu, K. M. Chua, L. L. Wai, J. Lee, and J. Kim, "Double-stacked EBG structure for wideband suppression of simultaneous switching noise in LTCC-based SiP applications," IEEE Microw. Wirel. Compon. Lett. **16**(9), 481–483 (2006).

[28]Y. Peng, B. M. F. Rahman, X. Wang *et al.*, "Performance enhanced miniaturized and electrically tunable patch antenna with patterned permalloy based magneto-dielectric substrate," J. Appl. Phys. **115**, 17A505 (2014).

[29]A. Askarian, J. Yao, Z. Lu, and K. Wu, "Extremely low-profile periodic 2D leaky-wave antenna: An optimal solution for antenna-frontend integration," IEEE Trans. Antenn. Propag. **70**(9), 7798–7812 (2022).

[30]G. Lovat, P. Burghignoli, and D. R. Jackson, "Fundamental properties and optimization of broadside radiation from uniform leaky-wave antennas," IEEE Trans. Antenn. Propag. **54**(5), 1442–1452 (2006).

[31]A. Hosseini, F. Capolino, and F. De Flaviis, "Gain enhancement of a V-band antenna using a Fabry-Perot cavity with a self-sustained all-metal cap with FSS," IEEE Trans. Antenn. Propag. **63**(3), 909–921 (2015).

[32]D. R. Jackson *et al.*, "The fundamental physics of directive beaming at microwave and optical frequencies and the role of leaky waves," Proc. IEEE **99**(10), 1780–1805 (2011).

[33]M. M. Honari, P. Mousavi, and K. Sarabandi, "Miniaturized-element frequency selective surface metamaterials: A solution to enhance radiation of RFICs," IEEE Trans. Antenn. Propag. **68**(3), 1962–1972 (2020).

[34]Y. W. Hsu, H. C. Lin, and Y. C. Lin, "Modeling and PCB implementation of standing leaky-wave antennas incorporating edge reflection for broadside radiation enhancement," IEEE Trans. Antenn. Propag. **64**(2), 461–468 (2016).

[35]G. Lovat, P. Burghignoli, F. Capolino, and D. Jackson, "Highly-directive planar leaky-wave antennas: A comparison between metamaterial-based and conventional designs," Proc. Eur. Microw. Assoc. **12**, 12–21 (2006).

[36]M. U. Afzal and K. P. Esselle, "Quasi-analytical synthesis of continuous phase correcting structure to increase the directivity of circulary polarized Fabry-Perot resonator antennas," J. Appl. Phys. **117**, 214902 (2015).

[37]D. Zheng and K. Wu, "Leaky-wave antenna featuring stable radiation based on multimode resonator concept," IEEE Trans. Antenn. Propag. **68**(3), 2016–2030 (2020).

[38]A. Askarian and K. Wu, "Wideband and high-gain slot antenna using self-scalable current distribution and multi-mode resonance," in *IEEE 19th International Symposium on Antenna Technology and Applied Electromagnet (ANTEM)* (IEEE, 2021), pp. 1–2.

[39]Z. Zhang and F. Xiao, "An UWB bandpass filter based on a novel type of multimode resonator," IEEE Microw. Wirel. Compon. Lett. **22**(10), 506–508 (2012).

[40]C. H. Lee, C. I. G. Hsu, and C. J. Chen, "Band-notched balanced UWB BPF with stepped-impedance slotline multi-mode resonator," IEEE Microw. Wirel. Compon. Lett. **22**(4), 182–184 (2012).

[41]M. Poveda-Garcia and J. L. Gómez-Tornero, "Spectral analysis of broadband Fabry-Perot antennas with multiple coupled cavities," IEEE Trans. Antenn. Propag. **70**, 167–179 (2022).

[42]R. E. Collin, "Impedance transformation and matching," in *Foundations for Microwave Engineering* (IEEE, 2001), pp. 303–393.

[43]D. Pozar, "Considerations for millimeter wave printed antennas," IEEE Trans. Antenn. Propag. **31**(5), 740–747 (1983).

[44]A. T. Almutawa *et al.*, "Leaky-wave analysis of wideband planar Fabry-Pérot cavity antennas formed by a thick PRS," IEEE Trans. Antenn. Propag. **67**(8), 5163–5175 (2019).